Research Square

Preprints are preliminary reports that have not undergone peer review.
They should not be considered conclusive, used to inform clinical practice,
or referenced by the media as validated information.

Long-Wavelength Lorentz-Like Propagation in a Deformable Cellular Space

Shengliang Dong

dshljiayou@gmail.com

independepent researcher https://orcid.org/0009-0007-0074-6119

Research Article

Keywords: discrete spacetime, emergent Lorentz symmetry, stochastic homogenization, Poisson-Voronoi tessellation, dynamical geometry

Posted Date: August 28th, 2026

DOI: https://doi.org/10.21203/rs.3.rs-10834615/v1

License: This work is licensed under a Creative Commons Attribution 4.0 International License.
Read Full License

Additional Declarations: The authors declare no competing interests.

Long-Wavelength Lorentz-Like Propagation in a Deformable Cellular Space

Shengliang Dong[1*]

[1*]Independent Researcher, Chengdu, 610500, Sichuan, China.

Corresponding author(s). E-mail(s): dshljiayou@gmail.com;

Abstract

Spatial discreteness generically supplies preferred microscopic directions, whereas a relativistic long-wave sector requires an isotropic propagation cone. We examine this tension in a classical kinematical model of mobile Voronoi cells carrying compact internal phases. Linearization about a uniform phase vacuum gives a face-area-weighted graph wave equation. For each periodic realization, a discrete corrector problem determines the quadratic coefficient of the lowest Bloch branch. We prove the following conditional statement: if the stationary ergodic marked-cell ensemble admits a deterministic, finite, positive-definite homogenized tensor, rotational invariance of its law forces that tensor to equal $\boldsymbol{c_0}\mathbb{I}$. The two-derivative phase action then has one isotropic limiting speed. In 88 independent Poisson–Voronoi realizations with $\mathbf{8} \le \boldsymbol{N} \le \mathbf{216}$, the mean relative eigenvalue spread decreases from $\mathbf{0.2159}$ (95% bootstrap interval $[\mathbf{0.1829}, \mathbf{0.2524}]$) to $\mathbf{0.0391}$ ($[\mathbf{0.0324}, \mathbf{0.0454}]$). Direct Metropolis sampling of two finite-modulus measures gives anisotropies $\mathbf{0.1110}$ and $\mathbf{0.1063}$, consistent with independent importance-reweighted estimates ($|\boldsymbol{z}| < \mathbf{0.23}$). Direct Bloch diagonalization also recovers the corrector coefficients as $\boldsymbol{k\ell} \to \mathbf{0}$, while finite-cell corrections enter at fourth derivative order. These results establish a controlled route to Lorentz-like propagation in the two-derivative phase sector; they do not establish microscopic boost invariance or a universal cone for geometric modes.

Keywords: discrete spacetime, emergent Lorentz symmetry, stochastic homogenization, Poisson–Voronoi tessellation, dynamical geometry

1 Introduction

If spacetime has a discrete microscopic structure, its local elements must reproduce the observed absence of a preferred propagation direction at accessible scales, as emphasized by increasingly stringent Lorentz tests [1–4]. This problem appears in different forms in Regge calculus, causal sets, causal dynamical triangulations, spin networks, and graph-based models of quantum geometry [5–14]. A regular spatial lattice makes locality transparent but also supplies fixed axes. Exact cellular automata can recover relativistic field equations in special constructions [15, 16], while random discretizations avoid a persistent crystalline frame [17, 18]. The general issue remains to identify which properties of a discrete substrate are sufficient for an isotropic limiting cone and which microscopic corrections survive coarse graining.

Two features are often treated separately. First, the propagation operator must homogenize to an isotropic continuum operator. Random-conductance and Delaunay-graph invariance principles provide the mathematical precedent that stationary random networks can converge to Brownian, rotationally invariant transport [19–29].

Second, if the discrete elements are interpreted physically rather than as a regulator, their geometry cannot be a permanently rigid ether. Local elements should be able to move, deform, and change neighbours while the interaction energy remains well defined. Voronoi geometry provides both a spatial partition and an adjacency graph derived from the instantaneous generator positions [30–36]. Related Voronoi and vertex models demonstrate that finite volume and surface penalties can coexist with rearranging neighbours in deformable cellular systems [37–44].

Here these two requirements are combined in one conservative model. A periodic Voronoi tessellation represents deformable cells. Each cell carries three compact internal phases; a face-area-weighted interaction transmits a phase perturbation and exerts the reciprocal force on the cell generators. The present paper concentrates on the propagation question. Starting from the discrete action, we derive the long-wave coefficient by solving the periodic corrector problem for the weighted graph. The derivation separates three logically distinct statements: one realization has a tensorial limiting speed; a statistically isotropic ensemble has a scalar ensemble limit; and a finite realization approaches that limit with measurable directional fluctuations. This separation is essential because the usual plane-wave Rayleigh quotient on an irregular graph is only an affine trial value, not its true lowest-branch eigenvalue.

The central question is therefore not whether a single irregular cell is isotropic, but whether the relaxed long-wave operator has a scalar deterministic limit. Conditional on the existence of a finite, positive-definite homogenized tensor for the exact face-area conductance law, stationarity, ergodicity, and rotational invariance imply

$$S_{\mathrm{eff}} = \frac{1}{2}\int \mathrm{d}t\,\mathrm{d}^3x\,\left[Z_t(\partial_t\phi)^2 - Z_s|\nabla\phi|^2 - m^2\phi^2\right] + O(\ell^2\partial^4), \tag{1}$$

for each linear internal component. After a constant rescaling of time, its two-derivative part has the Klein–Gordon form with $c_{\mathrm{eff}}^2 = Z_s/Z_t$. We separate this theorem from two numerical tests: finite-size Poisson–Voronoi ensembles probe the approach to a scalar tensor, and direct finite-modulus Metropolis chains test the earlier importance- reweighting approximation. Fourth-order terms retain the cell scale ℓ. Similar two-scale separations occur in analogue-spacetime models, although the cellular variables and corrector problem used here are different [45].

2 Dynamical cellular model

2.1 Geometry and internal variables

Let Ω be a flat periodic three-torus containing N distinct generators $\boldsymbol{X}_i(t)$. They define the instantaneous Voronoi cells

$$C_i = \{\boldsymbol{x} \in \Omega : |\boldsymbol{x} - \boldsymbol{X}_i| \le |\boldsymbol{x} - \boldsymbol{X}_j| \text{ for all } j\}. \tag{2}$$

We write V_i and S_i for their volumes and surface areas. If C_i and C_j share a face, its area is $A_{ij} > 0$. The geometric energy is

$$U_{\mathrm{geo}} = \sum_i \left[\frac{K_V}{2}(V_i - V_0)^2 + \frac{K_S}{2}(S_i - S_0)^2\right]. \tag{3}$$

It makes the cells deformable: volume and surface variations cost finite energy, but no global lattice sites are imposed.

Cell i also carries three phases $\boldsymbol{\theta}_i = (\theta_{i1}, \theta_{i2}, \theta_{i3}) \in (S^1)^3$. With a reference area $\bar{A}$, their energy is

$$U_{\mathrm{int}} = J\sum_{i\sim j}\frac{A_{ij}}{\bar{A}}\sum_{r=1}^{3}[1 - \cos(\theta_{ir} - \theta_{jr})] + \kappa\sum_{i,r}[1 - \cos(3\theta_{ir})]. \tag{4}$$

The on-site term selects three values for each phase component, giving 27 uniform vacua. Their multiplicity is an internal property and is unrelated to the number of spatial cells N, which is arbitrary. The threefold term is the standard clock anisotropy of a compact phase, although no critical clock-model result is assumed here [46].

The conservative action is

$$\mathcal{S} = \int \mathrm{d}t\left[\sum_i \frac{M}{2}|\dot{\boldsymbol{X}}_i|^2 + \sum_{i,r}\frac{I}{2}\dot{\theta}_{ir}^2 - U_{\mathrm{geo}} - U_{\mathrm{int}}\right]. \tag{5}$$

The parameter t is calibrated operationally by the internal oscillation period. A state with vanishing

ensemble momentum has no mean cellular drift; individual generators may nevertheless fluctuate or rearrange locally. The separation between the propagation time and the slow background evolution is expressed by $\omega\tau_X \gg 1$, where τ_X is the characteristic time over which the geometry changes appreciably. The frozen-geometry equations below are the leading term of this adiabatic regime.

On an infinite domain, or before taking a periodic finite-volume regulator, Eqs. (3)–(5) are equivariant under a common spatial rotation of all positions and momenta. This gives a useful distinction between mobile cells and a flowing medium with an imposed velocity.

Proposition 1 (Preservation of statistical isotropy) *Let a phase-space probability density be invariant under common spatial rotations and have zero mean total momentum. Wherever the Hamiltonian flow of Eq. (5) is defined, its time-evolved density retains both properties.*

Proof The Hamiltonian commutes with the action of $SO(3)$ and conserves total momentum. Its flow therefore commutes with every common rotation. Pushing forward a rotation-invariant density by this equivariant flow leaves it rotation invariant, while momentum conservation keeps its mean equal to zero. □

A finite cubic torus reduces exact rotations to its point group; the full statement concerns the infinite-volume ensemble represented by increasing periodic boxes.

2.2 Linear phase operator

Choose any uniform vacuum and write $\theta_{ir} = 2\pi q_r/3 + \vartheta_{ir}$. To quadratic order,

$$U_{\mathrm{int}}^{(2)} = \frac{J}{2}\sum_{i\sim j,r} w_{ij}(\vartheta_{ir}-\vartheta_{jr})^2 + \frac{9\kappa}{2}\sum_{i,r}\vartheta_{ir}^2, \qquad w_{ij} = \frac{A_{ij}}{\bar{A}}. \tag{6}$$

All three components obey the same weighted graph equation

$$I\ddot{\vartheta}_i + 9\kappa\vartheta_i + J(L_w\vartheta)_i = 0, \qquad (L_w f)_i = \sum_{j\sim i} w_{ij}(f_i - f_j). \tag{7}$$

At a uniform vacuum, the mixed geometry–phase Hessian vanishes because the first derivative of every bond factor $1-\cos\Delta\theta$ is zero. Thus the linear phase branch can be derived on a frozen cellular snapshot even though nonuniform states couple reciprocally to the moving geometry.

3 Homogenized propagation cone

3.1 Periodic cell problem

Consider one periodic realization. For each directed face $e = (i, j, \boldsymbol{n})$, let

$$\boldsymbol{d}_e = \boldsymbol{X}_j + \boldsymbol{n}L - \boldsymbol{X}_i, \tag{8}$$

where $\boldsymbol{n}$ labels the periodic image. A Bloch perturbation has the form $\vartheta_i(t) = u_i(\boldsymbol{k})e^{\mathrm{i}\boldsymbol{k}\cdot\boldsymbol{X}_i - \mathrm{i}\omega t}$. The lowest eigenvalue $\lambda_0(\boldsymbol{k})$ of the Hermitian Bloch Laplacian satisfies

$$\omega^2(\boldsymbol{k}) = \Omega_0^2 + \frac{J}{I}\lambda_0(\boldsymbol{k}), \qquad \Omega_0^2 = \frac{9\kappa}{I}. \tag{9}$$

The coefficient of its long-wave expansion follows from a periodic corrector $\boldsymbol{\chi}_i \in \mathbb{R}^3$. For an imposed macroscopic gradient $\boldsymbol{g}$, define

$$\boldsymbol{g}\cdot C^{\mathrm{eff}}\boldsymbol{g} = \min_{\{\chi_i\}} \frac{1}{2N}\sum_e w_e[\boldsymbol{g}\cdot\boldsymbol{d}_e + \boldsymbol{g}\cdot(\boldsymbol{\chi}_j - \boldsymbol{\chi}_i)]^2. \tag{10}$$

The sum is over directed faces, and one corrector value is fixed to remove the constant null mode. Equation (10) is a finite, positive-semidefinite quadratic minimization. It is equivalent to solving three weighted graph Poisson equations. Allowing the corrector is necessary: setting $\boldsymbol{\chi}_i = 0$ gives a plane-wave Rayleigh quotient and therefore only an upper bound on the lowest-branch coefficient of an irregular graph.

Proposition 2 (Long-wave propagation tensor) *For a connected periodic weighted cell graph with positive face weights,*

$$\lambda_0(\boldsymbol{k}) = k_a C_{ab}^{\mathrm{eff}} k_b + O(|\boldsymbol{k}|^4) \tag{11}$$

as $\boldsymbol{k}\to 0$, with C^{eff} given by Eq. (10).

Proof The eigenvector at $\boldsymbol{k} = 0$ is constant. Write its analytic continuation as $u_i(\boldsymbol{k}) = N^{-1/2}[1 + \mathrm{i}\boldsymbol{k}\cdot$

$\boldsymbol{\chi}_i + O(k^2)]$ and insert it in the Bloch quadratic form. Expanding $e^{\mathrm{i}\boldsymbol{k}\cdot\boldsymbol{d}_e}$ to second order produces the expression minimized in Eq. (10). Stationarity with respect to each $\boldsymbol{\chi}_i$ is precisely the order-k eigenvector equation. Substitution therefore gives Eq. (11); inversion symmetry of the directed-face set removes odd powers. □

3.2 Statistical isotropy

Let the generator process be stationary, ergodic, and invariant in law under every $R \in SO(3)$, with nondegenerate three-dimensional connectivity and the moment bounds required by stochastic homogenization. Rotating a realization maps its effective tensor to $RC^{\mathrm{eff}}R^{\mathsf{T}}$. We assume that the finite-volume tensors converge almost surely to a deterministic positive tensor C_{hom}; random-conductance and Delaunay invariance principles give conditions under which such nondegenerate limits exist [22, 26, 28, 29].

Proposition 3 (Conditional isotropic homogenized cone) *Let the stationary ergodic marked Voronoi ensemble have a deterministic, finite, positive-definite homogenized conductance tensor C_{hom}. If its law is invariant under $SO(3)$ and the conductance rule is rotation covariant, then*

$$C_{\mathrm{hom}} = c_0\mathbb{I}, \qquad c_0 > 0. \tag{12}$$

Consequently the two-derivative phase action has a single isotropic limiting speed after a constant rescaling of time.

Proof Rotational invariance implies $RC_{\mathrm{hom}}R^{\mathsf{T}} = C_{\mathrm{hom}}$ for every $R \in SO(3)$. The commutant of the defining three-dimensional rotation representation consists of scalar matrices, hence $C_{\mathrm{hom}} = c_0\mathbb{I}$. The assumed positive definiteness gives $c_0 > 0$. □

Existence and nondegeneracy of C_{hom} are assumptions here for the exact face-area conductance law. The proposition identifies the tensor's form once that homogenized limit exists; it is not an existence theorem for this particular correlated Voronoi weight distribution.

After coarse graining one cell volume into d^3x, Eqs. (9) and (12) give

$$\partial_t^2\phi - c_{\mathrm{eff}}^2\nabla^2\phi + \Omega_0^2\phi = O(\ell^2\partial^4\phi). \tag{13}$$

The two-derivative part is invariant under Lorentz transformations with limiting speed c_{eff}. The cellular scale ℓ enters through the fourth-order tensor. On a regular cubic graph, for example,

$$\lambda(\boldsymbol{k}) = a^2|\boldsymbol{k}|^2 - \frac{a^4}{12}\sum_{\mu=1}^{3}k_\mu^4 + O(a^6k^6), \tag{14}$$

which displays the microscopic directional dependence explicitly.

This statement is stronger than spatial isotropy alone but narrower than microscopic boost invariance. In the effective phase theory, time and space derivatives occur at quadratic order only through the Minkowski operator $\partial_t^2 - c_{\mathrm{eff}}^2\nabla^2$, so correlation functions constructed from this free sector transform covariantly under boosts defined with c_{eff}. The microscopic rest ensemble becomes observable through the $O(\ell^2\partial^4)$ coefficients, through nonadiabatic geometry–phase couplings, or through another sector with a different limiting speed. These are the three operational tests of Lorentz emergence in the present model.

4 Finite-volume test on random cellular spaces

4.1 Ensemble and numerical method

We generated binomial point processes (Poisson processes conditioned on a fixed point count) of unit number density on a three-torus for $N = 8, 27, 64, 125$, and 216. The sample counts were 20, 20, 20, 16, and 12, respectively, for a total of 88 independent realizations. In infinite space this process is statistically isotropic; the cubic torus is its finite-volume periodic approximation and retains only cubic symmetry. The samples also give the free-generator equilibrium baseline of the action when $K_V = K_S = 0$: in a uniform internal vacuum the canonical positional density is constant, so conditioning on N gives independent uniform generators. Their Maxwellian momenta may be taken at sufficiently low temperature to satisfy $\omega\tau_X \gg 1$ without altering that positional marginal. Finite-modulus equilibrium ensembles were sampled separately as described below. A $3 \times 3 \times 3$ periodic image construction supplied every central Voronoi volume and face. The sum of cell volumes agreed with the box volume to relative error below

3×10^{-16} in all samples. Numerical units set the mean cell volume, $\bar{A}$, and ℓ to one.

We first tested weak geometric stiffness by evaluating 16 additional $N = 27$ configurations and importance-reweighting them by

$$W = \exp[-\beta K_V \mathcal{V} - \beta K_S \mathcal{S}],$$
$$\mathcal{V} = \tfrac{1}{2}\sum_i (V_i - 1)^2, \qquad \mathcal{S} = \tfrac{1}{2}\sum_i (S_i - S_0)^2, \tag{15}$$

where $S_0 = 5.315$ is the surface area of a unit-volume BCC Voronoi cell. Reliability was monitored with $N_{\mathrm{eff}} = (\sum W)^2 / \sum W^2$.

We then sampled each weighted measure directly with four independent Metropolis chains. A proposal displaces one generator by a wrapped Gaussian step, after which the complete periodic Voronoi volumes and surface areas are recomputed. Both parameter pairs used 800 burn-in proposals, 40 retained configurations per chain, and 27 proposals between retained configurations. The proposal scale was 1.5 mean cell lengths. Acceptance rates were 0.924–0.940 for $(\beta K_V, \beta K_S) = (0.5, 0.02)$ and 0.851–0.869 for $(1, 0.05)$; no proposal failed the periodic geometry construction. Uncertainty for direct estimates was obtained by bootstrapping the four chain means, rather than treating the 160 retained rows as independent.

For each realization we assembled the directed weighted graph, solved the three corrector systems in Eq. (10), and diagonalized C^{eff}. We quantify the finite-volume directional splitting by

$$\mathcal{A}_2 = \frac{C_3 - C_1}{(C_1 + C_2 + C_3)/3}, \qquad C_1 \le C_2 \le C_3. \tag{16}$$

Confidence intervals in Fig. 1 are nonparametric 95% bootstrap intervals for the sample mean; all individual realizations are shown.

4.2 Convergence and direct spectral check

Table 1 reports the ensemble results. The mean anisotropy decreases by a factor of 5.5 between $N = 8$ and $N = 216$. Its 95% mean interval at $N = 216$, $[0.0324, 0.0454]$, lies well below the interval at $N = 8$, $[0.1829, 0.2524]$. All three coefficient scales remain finite and approach values of order 1.1. These data support finite-volume restoration of rotational isotropy but are not used to fit an asymptotic exponent.

The unweighted anisotropy in the independent $N = 27$ control set is 0.1167. Importance reweighting gives 0.11081 with $N_{\mathrm{eff}} = 13.3$ at $(0.5, 0.02)$ and 0.10795 with $N_{\mathrm{eff}} = 9.6$ at $(1, 0.05)$. Direct chains give 0.11101 (chain-block 95% interval $[0.10671, 0.11512]$) and 0.10628 ($[0.10249, 0.11045]$), respectively. Combining the direct and reweighted bootstrap standard errors gives standardized discrepancies $z = 0.027$ and $z = -0.227$. Thus the independent samplers agree at both tested moduli. This agreement does not validate extrapolation to strong penalties: reweighting to $(10, 1)$ has $N_{\mathrm{eff}} = 1.03$ and is unusable.

As an independent check, we assembled the full complex Bloch matrix for one $N = 64$ realization and diagonalized it along the three principal directions of its cell-problem tensor. Figure 2 shows that $\lambda_0(\boldsymbol{k})/k^2$ approaches the corresponding C_a in every direction as $k\ell \to 0$; at the smallest sampled value $k\ell = 0.012$, all three relative differences are below 2.3×10^{-5}. The downward curvature at $k\ell \gtrsim 0.1$ resolves the finite-cell correction rather than a change in the limiting tensor. Fitting $\lambda_0/k^2 = C_a + D_a(k\ell)^2$ over $k\ell \le 0.2$ gives $D_a = (-0.155, -0.153, -0.179)$; each fitted intercept agrees with the independent C_a within 1.8×10^{-6} relatively. These coefficients are a prediction for the displayed realization, not an ensemble universal.

5 Mobility, adjacency changes, and applicability

The preceding homogenization is instantaneous: it applies over a wave period when the generator geometry changes adiabatically. Mobility enters the same action through Eq. (3) and through the dependence $A_{ij}(\boldsymbol{X})$. A nonuniform phase field therefore exerts a force

$$-\frac{J}{\bar{A}} \sum_{i \sim j} \frac{\partial A_{ij}}{\partial \boldsymbol{X}_\ell} [1 - \cos(\theta_i - \theta_j)] \tag{17}$$

on generator ℓ. The background is not a prescribed global rest lattice: its local rest state and its weighted propagation tensor evolve with the cellular configuration.

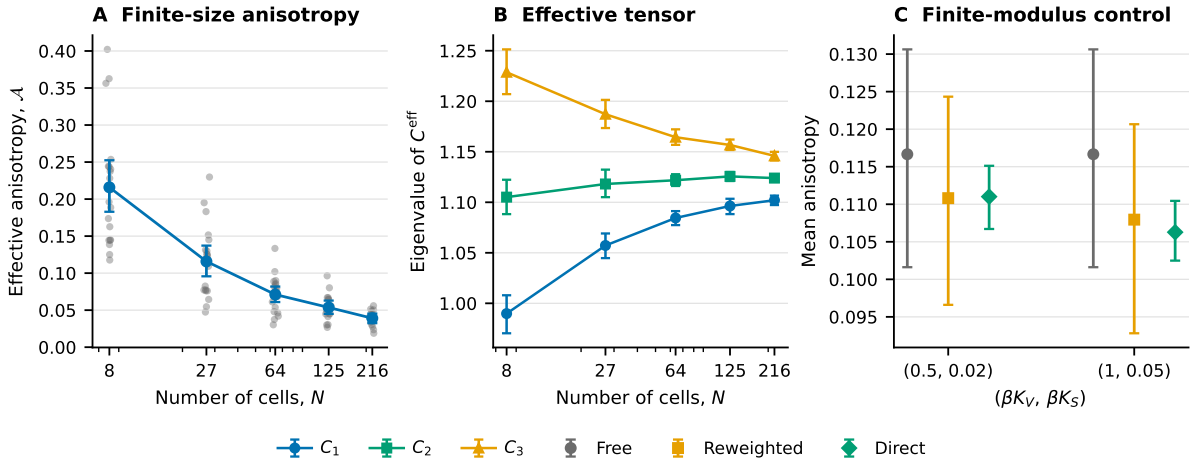


Fig. 1 Finite-volume and finite-modulus tests. **A**, individual Poisson–Voronoi anisotropies and 95% bootstrap intervals for their mean. **B**, the three eigenvalues of C^{eff} with corresponding mean intervals. **C**, free, importance-reweighted, and directly sampled $N = 27$ estimates. Direct intervals bootstrap four independent chain means; the other intervals bootstrap the 16 independent free configurations.

Table 1 Poisson–Voronoi tensor statistics. Brackets are nonparametric 95% bootstrap intervals for the mean.

N	n_s	$\langle \mathcal{A}_2 \rangle$	$\langle C_1 \rangle$	$\langle C_3 \rangle$
8	20	0.2159 [0.1829, 0.2524]	0.9898 [0.9703, 1.0080]	1.2287 [1.2070, 1.2513]
27	20	0.1158 [0.0957, 0.1372]	1.0572 [1.0447, 1.0691]	1.1872 [1.1735, 1.2013]
64	20	0.0711 [0.0610, 0.0819]	1.0845 [1.0774, 1.0913]	1.1644 [1.1568, 1.1722]
125	16	0.0537 [0.0450, 0.0629]	1.0963 [1.0883, 1.1035]	1.1567 [1.1518, 1.1621]
216	12	0.0391 [0.0324, 0.0454]	1.1020 [1.0973, 1.1066]	1.1459 [1.1414, 1.1499]

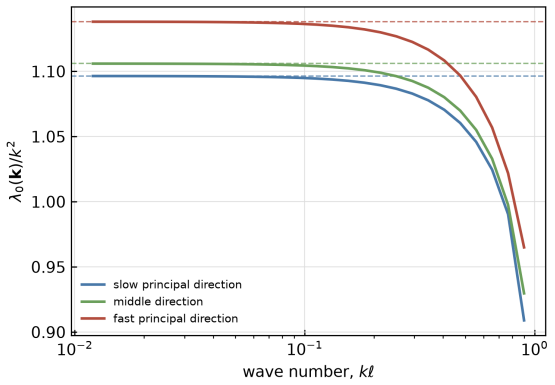


Fig. 2 Lowest Bloch eigenvalue of a 64-cell Poisson–Voronoi realization along the principal directions of C^{eff}. Dashed lines are the independently calculated cell-problem coefficients. The direct spectrum reaches these limits at small wave number and resolves discrete corrections at shorter wavelength.

When a generic Voronoi face disappears, $A_{ij} \to 0$. Its interaction energy obeys

$$0 \le \frac{JA_{ij}}{\bar{A}}[1 - \cos(\Delta\theta)] \le \frac{2JA_{ij}}{\bar{A}} \longrightarrow 0. \qquad (18)$$

The propagation operator is therefore energy-continuous through a neighbour exchange. This property distinguishes a dynamical cellular substrate from a fixed ether lattice, while leaving short-time propagation governed by the instantaneous weighted graph.

As a dynamical check of this statement, we evolved one $N = 64$ free-generator sample ballistically on the torus with isotropic random velocities adjusted to zero total momentum. Across 25 snapshots, all 24 successive intervals changed the adjacency set (the accumulated edge-set symmetric difference was 739). The instantaneous anisotropy remained between 0.044 and 0.126 and the three propagation coefficients stayed finite. This single trajectory is not an ensemble convergence test; it verifies that repeated neighbour changes do not interrupt the tensor construction or generate a cumulative singularity.

Equation (13) also gives the model's phenomenological boundary. At momentum $p\ell \ll 1$, the fractional modification of the quadratic branch is of order $(p\ell)^2$; finite regions add a stochastic

directional splitting measured by Eq. (16). A signal would therefore be an energy-dependent propagation correction correlated with fourth-order angular structure, rather than a constant preferred-frame velocity. Bounds on Lorentz-violating dispersion constrain combinations of ℓ and the fourth-order tensor [1, 2]; they do not determine the microscopic cell scale without specifying how the phase mode couples to an observed field.

The conditional common limiting cone belongs to the three degenerate phase components. Geometric displacement modes derive from the Hessian of U_{geo} and generally have longitudinal and transverse elastic speeds. For an isotropic elastic continuum they obey

$$c_L^2 = \frac{K + 4\mu/3}{\rho}, \qquad c_T^2 = \frac{\mu}{\rho}, \tag{19}$$

where K and μ are the bulk and shear moduli.

Proposition 4 (Elastic common-cone obstruction) *A stable conventional isotropic elastic sector with $K > 0$ and $\mu > 0$ cannot have $c_L = c_T$.*

Proof Equation (19) gives $c_L^2 - c_T^2 = (K + \mu/3)/\rho > 0$. □

A universal cone shared by phase and geometric excitations therefore cannot be obtained by tuning positive elastic moduli alone. It requires the geometric variables to acquire an additional constraint or gauge structure, or not to represent independent observable matter modes. This is the common-cone and radiative-stability problem familiar in other approaches to emergent Lorentz symmetry [47–50]. The cellular construction isolates that condition rather than hiding it inside a regular-lattice ansatz.

6 Discussion

The numerical and analytic results answer a focused question: microscopic spatial discreteness does not by itself force a persistent macroscopic propagation axis. The relevant object is the homogenized second-rank tensor, not the orientation of any one face or cell. If a nondegenerate homogenized limit exists, statistical rotational invariance makes this tensor scalar, and the discrete graph wave equation then produces the Klein–Gordon operator at two derivatives. Finite-size anisotropy and fourth-order dispersion remain and can be calculated from the same microscopic geometry.

An isotropic material can also support a wave equation in its rest frame, so the word "isotropic" alone would not establish observer equivalence. Here the Lorentz-like statement is tied to the complete quadratic phase action: after one time rescaling it contains no independent background vector or directional coefficient. Observer-dependent effects reappear in the explicitly calculated higher-derivative tensor. This effective-symmetry criterion is the reason the conclusion is restricted to the long-wave phase sector rather than attributed to the full microscopic cellular dynamics.

Randomness plays a precise role. It is not invoked to average away an arbitrary violation after the fact. It defines an invariant ensemble, while the corrector problem accounts for local field relaxation inside each realization. This is why a simple angular average of bond vectors would be insufficient. The direct Bloch calculation verifies the corrector result and shows where the continuum approximation loses accuracy.

Mobility and isotropy are compatible but logically different. Mobility prevents the cellular elements from constituting a permanently fixed frame; zero ensemble momentum and rotationally invariant statistics determine the background used for propagation. Slow cellular evolution makes the coefficients in Eq. (13) local functions of space and time. Rapid background evolution would require a two-time homogenization and would generate additional scattering or damping terms. The adiabatic condition $\omega\tau_X \gg 1$ marks the domain in which the conservative effective wave equation derived here applies.

7 Conclusion

We constructed a deformable Voronoi cellular model and derived the quadratic propagation tensor of its internal phase branch from a periodic corrector problem. Provided the exact weighted ensemble has a deterministic, positive-definite homogenized limit, rotational invariance forces that limit to be scalar. Expanded Poisson–Voronoi ensembles show a strong reduction of finite-volume directional splitting, direct finite-modulus chains agree with importance reweighting, and Bloch spectra recover the corrector coefficients at

long wavelength. Face-area weighting also keeps the bond energy continuous through neighbour changes. Together these results show that a discrete, rearrangeable spatial substrate can possess a Lorentz-like two-derivative phase sector without a rigid lattice axis. Establishing the homogenization hypotheses for the correlated face-area law, treating rapid geometry evolution, and obtaining a common cone for additional sectors remain separate problems.

Declarations

Funding

The author received no funding for this work.

Competing interests

The author declares no competing interests.

Data availability

All numerical data underlying the figures are supplied with the manuscript.

Code availability

The source code used to construct the periodic Voronoi geometries, solve the cell problems, and diagonalize the Bloch kernels is supplied with the manuscript.

Supplementary numerical information

The periodic tessellation is reconstructed with SciPy/Qhull from 27 image boxes, retaining the cells whose generators lie in the central box. Every physical interface is represented by two directed faces and is divided by two in the quadratic form. Three gauge-fixed graph Poisson systems yield the correctors in Eq. (10). The Bloch check constructs the full $N \times N$ Hermitian matrix from the same directed faces and evaluates its lowest eigenvalue. Automated tests include the exact cubic-lattice tensor and dispersion, the small-k agreement between the Bloch eigenvalue and cell problem, positivity of the corrector reduction, deterministic point generation, and periodic box containment. Figure data are stored as CSV files with the ensemble type, cell count, random seed, three tensor eigenvalues, anisotropy, and volume-closure residual for every realization. The supplementary free-generator trajectory additionally records time, instantaneous eigenvalues, anisotropy, and adjacency-set changes. The reweighting file stores the volume and surface costs separately so that all reported weights and effective sample sizes can be reconstructed. The direct finite-modulus archive contains four chains per parameter pair, including seeds, cumulative acceptance rates, tensor eigenvalues, volume closure, and adjacency counts. The finite-size figure is generated only from archived CSV files; its plotted-value table records every mean, interval, effective sample size, and standardized direct–reweighted discrepancy.

Author contributions

The author conceived the model, performed the analysis and numerical work, and wrote the manuscript.

References

[1] Mattingly, D.: Modern tests of Lorentz invariance. Living Reviews in Relativity **8**(1), 5 (2005) https://doi.org/10.12942/lrr-2005-5

[2] Liberati, S.: Tests of Lorentz invariance: a 2013 update. Classical and Quantum Gravity **30**(13), 133001 (2013) https://doi.org/10.1088/0264-9381/30/13/133001

[3] Tasson, J.D.: What do we know about Lorentz invariance? Reports on Progress in Physics **77**(6), 062901 (2014) https://doi.org/10.1088/0034-4885/77/6/062901

[4] Addazi, A., *et al.*: Quantum gravity phenomenology at the dawn of the multi-messenger era—a review. Progress in Particle and Nuclear Physics **125**, 103948 (2022) https://doi.org/10.1016/j.ppnp.2022.103948

[5] Regge, T.: General relativity without coordinates. Il Nuovo Cimento **19**, 558–571 (1961) https://doi.org/10.1007/BF02733251

[6] Bombelli, L., Lee, J., Meyer, D., Sorkin, R.D.: Space-time as a causal set. Physical Review Letters **59**, 521–524 (1987) https://doi.org/10.1103/PhysRevLett.59.521

[7] Rideout, D.P., Sorkin, R.D.: Classical sequential growth dynamics for causal sets. Physical Review D **61**, 024002 (2000) https://doi.org/10.1103/PhysRevD.61.024002

[8] Ambjorn, J., Jurkiewicz, J., Loll, R.: Dynamically triangulating lorentzian quantum gravity. Nuclear Physics B **610**, 347–382 (2001) https://doi.org/10.1016/S0550-3213(01)00297-8

[9] Loll, R.: Quantum gravity from causal dynamical triangulations: a review. Classical and Quantum Gravity **37**, 013002 (2020) https://doi.org/10.1088/1361-6382/ab57c7

[10] Rovelli, C., Smolin, L.: Spin networks and quantum gravity. Physical Review D **52**, 5743–5759 (1995) https://doi.org/10.1103/PhysRevD.52.5743

[11] Rovelli, C.: Quantum Gravity. Cambridge University Press, Cambridge (2004). https://doi.org/10.1017/CBO9780511755804

[12] Konopka, T., Markopoulou, F., Smolin, L.: Quantum graphity. Physical Review D **77**, 104029 (2008) https://doi.org/10.1103/PhysRevD.77.104029

[13] Hamma, A., Markopoulou, F., Lloyd, S., Caravelli, F., Severini, S., Markstrom, K.: A quantum Bose–Hubbard model with an evolving graph as a toy model for emergent spacetime. Physical Review D **81**, 104032 (2010) https://doi.org/10.1103/PhysRevD.81.104032

[14] Finster, F.: From discrete space-time to minkowski space: Basic mechanisms, methods and perspectives. In: Quantum Field Theory: Competitive Models, pp. 235–259. Birkhauser, Berlin, Germany (2009). https://doi.org/10.1007/978-3-7643-8736-5_14

[15] Bialynicki-Birula, I.: Weyl, Dirac, and Maxwell equations on a lattice as unitary cellular automata. Physical Review D **49**, 6920–6927 (1994) https://doi.org/10.1103/PhysRevD.49.6920

[16] D'Ariano, G.M., Perinotti, P.: Derivation of the Dirac equation from principles of information processing. Physical Review A **90**, 062106 (2014) https://doi.org/10.1103/PhysRevA.90.062106

[17] Christ, N.H., Friedberg, R., Lee, T.D.: Random lattice field theory: General formulation. Nuclear Physics B **202**, 89–125 (1982) https://doi.org/10.1016/0550-3213(82)90222-X

[18] Bombelli, L., Henson, J., Sorkin, R.D.: Discreteness without symmetry breaking: a theorem. Modern Physics Letters A **24**, 2579–2587 (2009) https://doi.org/10.1142/S0217732309031958

[19] Kozlov, S.M.: The averaging of random operators. Mathematics of the USSR-Sbornik **37**(2), 167–180 (1980) https://doi.org/10.1070/SM1980v037n02ABEH001948

[20] Jikov, V.V., Kozlov, S.M., Oleinik, O.A.: Homogenization of Differential Operators and Integral Functionals. Springer, Berlin (1994). https://doi.org/10.1007/978-3-642-84659-5

[21] Pavliotis, G.A., Stuart, A.M.: Multiscale Methods: Averaging and Homogenization. Springer, New York (2008). https://doi.org/10.1007/978-0-387-73829-1

[22] Andres, S., Barlow, M.T., Deuschel, J.-D., Hambly, B.M.: Invariance principle for the random conductance model. Probability Theory and Related Fields **156**, 535–580 (2013) https://doi.org/10.1007/s00440-012-0435-2

[23] Barlow, M.T., Deuschel, J.-D.: Invariance principle for the random conductance model with unbounded conductances. The Annals of Probability **38**(1), 234–276 (2010) https://doi.org/10.1214/09-AOP481

[24] Berger, N., Biskup, M.: Quenched invariance principle for simple random walk on percolation clusters. Probability Theory and Related Fields **137**, 83–120 (2007) https://doi.org/10.1007/s00440-006-0498-z

[25] Mathieu, P., Piatnitski, A.: Quenched invariance principles for random walks on percolation clusters. Proceedings of the Royal Society A **463**, 2287–2307 (2007) https://doi.org/10.1098/rspa.2007.1876

[26] Rousselle, A.: Quenched invariance principle for random walks on Delaunay triangulations. Electronic Journal of Probability **20**, 1–32 (2015) https://doi.org/10.1214/EJP.v20-4006

[27] Gloria, A., Otto, F.: An optimal variance estimate in stochastic homogenization of discrete elliptic equations. The Annals of Probability **39**(3), 779–856 (2011) https://doi.org/10.1214/10-AOP571

[28] Biskup, M.: Recent progress on the random conductance model. Probability Surveys **8**, 294–373 (2011) https://doi.org/10.1214/11-PS190

[29] Armstrong, S., Kuusi, T., Mourrat, J.-C.: Quantitative Stochastic Homogenization and Large-Scale Regularity. Grundlehren der mathematischen Wissenschaften, vol. 352. Springer, Cham (2019). https://doi.org/10.1007/978-3-030-15545-2

[30] Aurenhammer, F.: Voronoi diagrams—a survey of a fundamental geometric data structure. ACM Computing Surveys **23**(3), 345–405 (1991) https://doi.org/10.1145/116873.116880

[31] Okabe, A., Boots, B., Sugihara, K., Chiu, S.N.: Spatial Tessellations: Concepts and Applications of Voronoi Diagrams, 2nd edn. Wiley, Chichester (2000). https://doi.org/10.1002/9780470317013

[32] Penrose, M.: Random Geometric Graphs. Oxford University Press, Oxford (2003). https://doi.org/10.1093/acprof:oso/9780198506263.001.0001

[33] Last, G., Penrose, M.: Lectures on the Poisson Process. Cambridge University Press, Cambridge (2017). https://doi.org/10.1017/9781316104477

[34] Torquato, S.: Random Heterogeneous Materials: Microstructure and Macroscopic Properties. Springer, New York (2002). https://doi.org/10.1007/978-1-4757-6355-3

[35] Du, Q., Faber, V., Gunzburger, M.: Centroidal voronoi tessellations: applications and algorithms. SIAM Review **41**(4), 637–676 (1999) https://doi.org/10.1137/S0036144599352836

[36] Springel, V.: E pur si muove: Galilean-invariant cosmological hydrodynamical simulations on a moving mesh. Monthly Notices of the Royal Astronomical Society **401**(2), 791–851 (2010) https://doi.org/10.1111/j.1365-2966.2009.15715.x arXiv:0901.4107

[37] Nagai, T., Honda, H.: A dynamic cell model for the formation of epithelial tissues. Philosophical Magazine B **81**(7), 699–719 (2001) https://doi.org/10.1080/13642810108205772

[38] Fletcher, A.G., Osterfield, M., Baker, R.E., Shvartsman, S.Y.: Vertex models of epithelial morphogenesis. Biophysical Journal **106**(11), 2291–2304 (2014) https://doi.org/10.1016/j.bpj.2013.11.4498

[39] Alt, S., Ganguly, P., Salbreux, G.: Vertex models: from cell mechanics to tissue morphogenesis. Philosophical Transactions of the Royal Society B: Biological Sciences **372**(1720), 20150520 (2017) https://doi.org/10.1098/rstb.2015.0520

[40] Bi, D., Lopez, J.H., Schwarz, J.M., Manning, M.L.: A density-independent rigidity transition in biological tissues. Nature Physics **11**, 1074–1079 (2015) https://doi.org/10.1038/nphys3471 arXiv:1409.0593

[41] Bi, D., Yang, X., Marchetti, M.C., Manning, M.L.: Motility-driven glass and jamming transitions in biological tissues. Physical Review X **6**, 021011 (2016) https://doi.org/10.1103/PhysRevX.6.021011 arXiv:1509.06578

[42] Merkel, M., Manning, M.L.: A geometrically controlled rigidity transition in a model for confluent 3d tissues. New Journal of Physics **20**, 022002 (2018) https://doi.org/10.1088/1367-2630/aaaa13 arXiv:1706.02656

[43] Sussman, D.M., Merkel, M.: No unjamming transition in a voronoi model of biological tissue. Soft Matter **14**(17), 3397–3403 (2018) https://doi.org/10.1039/C7SM02127E

[44] Jain, H.P., Voigt, A., Angheluta, L.: Robust statistical properties of T1 transitions in a multi-phase field model of cell monolayers. Scientific Reports **13**(1), 10096 (2023) https://doi.org/10.1038/s41598-023-37064-6

[45] Barceló, C., Liberati, S., Visser, M.: Analogue gravity. Living Reviews in Relativity **14**(1), 3 (2011) https://doi.org/10.12942/lrr-2011-3

[46] Jose, J.V., Kadanoff, L.P., Kirkpatrick, S., Nelson, D.R.: Renormalization, vortices, and symmetry-breaking perturbations in the two-dimensional planar model. Physical Review B **16**, 1217–1241 (1977) https://doi.org/10.1103/PhysRevB.16.1217

[47] Chadha, S., Nielsen, H.B.: Lorentz invariance as a low-energy phenomenon. Nuclear Physics B **217**, 125–144 (1983) https://doi.org/10.1016/0550-3213(83)90081-0

[48] Collins, J., Perez, A., Sudarsky, D., Urrutia, L., Vucetich, H.: Lorentz invariance and quantum gravity: An additional fine-tuning problem? Physical Review Letters **93**(19), 191301 (2004) https://doi.org/10.1103/PhysRevLett.93.191301

[49] Hořava, P.: Quantum gravity at a Lifshitz point. Physical Review D **79**(8), 084008 (2009) https://doi.org/10.1103/PhysRevD.79.084008

[50] Bednik, G., Pujolàs, O., Sibiryakov, S.: Emergent Lorentz invariance from strong dynamics: holographic examples. Journal of High Energy Physics **2013**(11), 64 (2013) https://doi.org/10.1007/JHEP11(2013)064